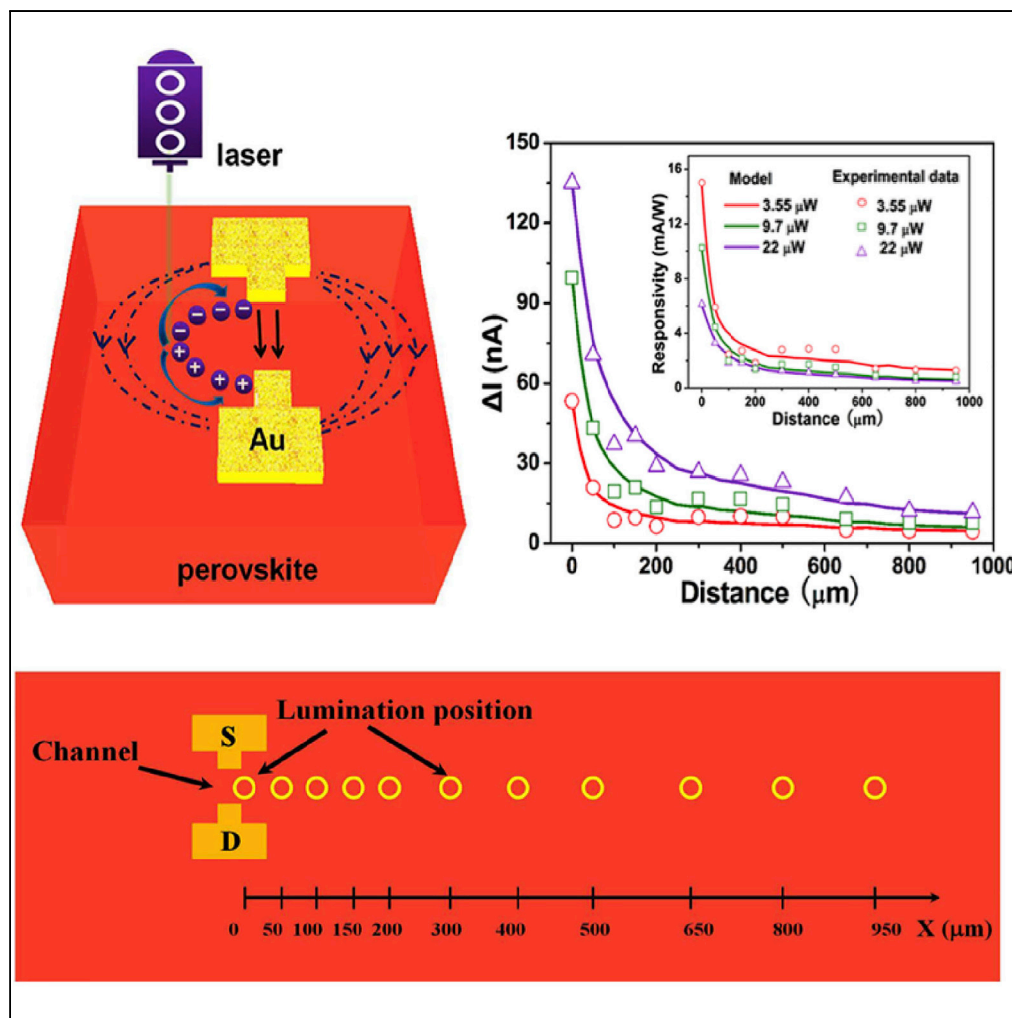


Article

Millimeter-Scale Nonlocal Photo-Sensing Based on Single-Crystal Perovskite Photodetector



Yu-Tao Li, Guang-Yang Gou, Lin-Sen Li, ..., Ping-Heng Tan, Yi Yang, Tian-Ling Ren

tianhe88@tsinghua.edu.cn (H.T.)
rentl@tsinghua.edu.cn (T.-L.R.)

HIGHLIGHTS

Position-dependent photodetector based on perovskite single crystals is fabricated

The photodetector demonstrates photo-sensing distance up to millimeter range

The attenuation of carrier diffusion length in $\text{CH}_3\text{NH}_2\text{PbBr}_3$ is revealed

Article

Millimeter-Scale Nonlocal Photo-Sensing Based on Single-Crystal Perovskite Photodetector

Yu-Tao Li,^{1,2,4} Guang-Yang Gou,^{1,2,4} Lin-Sen Li,^{1,2,4} He Tian,^{1,2,*} Xin Cong,³ Zhen-Yi Ju,^{1,2} Ye Tian,^{1,2} Xiang-Shun Geng,^{1,2} Ping-Heng Tan,³ Yi Yang,^{1,2} and Tian-Ling Ren^{1,2,5,*}

SUMMARY

Organometal trihalide perovskites (OTPs) are promising optoelectronic materials for high-performance photodetectors. However, up to now, traditional polycrystal OTP-based photodetectors have demonstrated limited effective photo-sensing range. Recently, bulk perovskite single crystals have been seen to have the potential for position-sensitive photodetection. Herein, for the first time, we demonstrate a position-dependent photodetector based on perovskite single crystals by scanning a focused laser beam over the device perpendicular to the channel. The photodetector shows the best-ever effective photo-sensing distance up to the millimeter range. The photoresponsivity and photocurrent decrease by nearly an order of magnitude when the beam position varies from 0 to 950 μm and the tunability of carrier diffusion length in $\text{CH}_3\text{NH}_2\text{PbBr}_3$ with the variation of the exciting laser intensity is demonstrated. Furthermore, a numerical model based on transport of photoexcited carriers is proposed to explain the position dependence. This photodetector shows excellent potential for application in future nanoelectronics and optoelectronics systems.

INTRODUCTION

Organometal trihalide perovskites (OTPs), a new family of optoelectronic materials, have recently attracted intense interest for photonic applications in photodetectors (Hu et al., 2014; Xia et al., 2014; Dou et al., 2014; Lee et al., 2015; Dong et al., 2015b; Fang and Huang, 2015; Li et al., 2015). Traditional OTP-based photodetectors based on solution-process polycrystalline OTP thin films show limited diffusion length ($\sim 1 \mu\text{m}$), resulting in many drawbacks in the photodetection performance (Saidaminov et al., 2015b; Stranks et al., 2013; Xing et al., 2013). Thus, there is an urgent need to search for alternative materials with low trap states, long charge carrier lifetime, and long carrier diffusion length for the improvement of photodetectors (Bi et al., 2016; Saidaminov et al., 2015b; Shi et al., 2015; Xing et al., 2013). Bulk perovskite single crystals with fewer grain boundaries are promising candidates with remarkable optoelectronic performances compared with traditional OTP thin films (Dong et al., 2015a; Ma et al., 2016; Saidaminov et al., 2015a; Shao et al., 2014; Shi et al., 2015; Yang et al., 2015; Zhang et al., 2016). Their excellent optoelectronic properties such as large absorption coefficient over a broad spectral range (Green et al., 2014), high charge carrier mobility ($60 \text{ cm}^{-2} \text{ V}^{-1} \text{ s}^{-1}$) (Saidaminov et al., 2015b; Shi et al., 2015), proper bandgap energy (2.2 eV) (Miyata et al., 2015), and long exciton diffusion length (7.5 μm) (Wei et al., 2016; Yang et al., 2015) have been exploited to realize high-sensitivity photo-sensing devices of different detection bands from X-ray to visible light (Fang et al., 2015; Mao et al., 2003; Saidaminov et al., 2015b). Besides, synthetic routes of bulk perovskite single crystals are very simple and rely on self-assembly, which offers the advantages of cost-effectiveness and large-scale manufacture (Dong et al., 2015a; Liu et al., 2015b; Yang et al., 2015). However, previously demonstrated OTP-based photodetectors only show a local photoresponse and the effective photo-sensing area in these devices is mainly the photodetector channel (Li et al., 2015; Saidaminov et al., 2015b) or the hybrid channel where OTPs are in contact with other photoactive nanomaterials (such as semiconductor [Dou et al., 2014; Wei et al., 2016], quantum dots [Liu et al., 2015a; Qian et al., 2017], or two-dimensional materials [Kang et al., 2016; Lee et al., 2015; Ma et al., 2016; Wang et al., 2015]). The position-dependent photodetectors based on perovskite single crystals have not been demonstrated yet, which leads to the insufficient development of its advantages in long diffusion length.

In many photo-sensing applications, illumination is not always precisely shining onto specific device locations, resulting in no photoresponse or a small response derived from a fraction of the illuminating power

¹Institute of Microelectronics, Tsinghua University, Beijing 100084, PR China

²Beijing National Research Center for Information Science and Technology (BNRist), Tsinghua University, Beijing 100084, PR China

³State Key Laboratory of Superlattices and Microstructures, Institute of Semiconductors, Chinese Academy of Sciences, Beijing 100083, PR China

⁴These authors contributed equally

⁵Lead Contact

*Correspondence: tianhe88@tsinghua.edu.cn (H.T.), rentl@tsinghua.edu.cn (T.-L.R.)

<https://doi.org/10.1016/j.isci.2018.08.021>



(Ghosh et al., 2010; Sarker et al., 2017). To overcome those limitations, it is of great importance to develop position-dependent photodetectors that can be operated without precise illumination on the device channel and to examine their position-dependent photoresponse characteristics. Up to now, very limited previous work has demonstrated position-dependent photodetectors by the combination of graphene and SiC substrate or using reduced graphene oxide (Sarker et al., 2017; Ghosh et al., 2010). However, the coupling of two materials (graphene and SiC) hinders photoelectric conversion efficiency and position dependence range (500 μm) of the device. Besides, bulk perovskite single crystals show larger single-crystal area compared with graphene, and the long carrier diffusion length allows the photo-generated charge carriers to be transported farther in perovskite single crystals, which provides potential for position-sensitive photodetection applications (Shi et al., 2015).

In this article, we use a single material, $\text{CH}_3\text{NH}_3\text{PbBr}_3$ (MAPbBr₃) single crystals, to realize the position-sensitive photodetectors. Hard mask and electron beam evaporation were utilized to define specifically shaped source and drain on the perovskite single crystals. By setting up a custom-designed optoelectronic test platform, the position-sensitive photoresponse characteristics of the photodetector was measured by a focused laser beam, showing both position sensitivity and large-area photodetection. This position-sensitive device presents local optoelectronic performance of an optimal responsivity of 51 mA/W, which is a reasonable value when compared with previous reports (Saidaminov et al., 2015b). A remarkable ratio of photocurrent and dark current of 9 indicates potential applications in the construction of integrated optoelectronic systems. Meanwhile, photoresponse can be achieved for laser illumination not only on the perovskite channel but also on the area millimeter range away from the device channel. Two more samples were fabricated to prove the repeatability of the experiment, and more details are shown in Figure S1. To the best of our knowledge, this is a record for millimeter-range distance detection. Finally, the position-sensitive photoresponse was qualitatively explained by finite element analysis based on the dependence of carrier diffusion and recombination under the change of electric field on the position of illumination near the device channel.

RESULTS

Based on high-quality single crystal MAPbBr₃, the position-dependent photodetector was fabricated (see Transparent Methods section for more details). The width and length of the perovskite channel are 150 and 120 μm , respectively. A schematic diagram of the position-dependent photodetector is shown in Figure 1A. The yellow parts and red substrate represent the Au pad and MAPbBr₃ crystal, respectively. Figure 1B shows the scanning electron micrograph of the device. The red line shown in Figure 1B is the direction of the laser spot movement while characterizing the photoresponse. The white part is the 50-nm-thick Au electrode deposited by electron beam evaporation, and the shape is regular. X-ray diffraction patterns of the crystals are investigated in Figure 1D. The strong diffraction peak at 14.9°, 30°, and 45.8° can be assigned to the (100), (200), and (300) planes, respectively, of pure perovskite phase for MAPbBr₃, indicating a good match with previously reported single crystals (Saidaminov et al., 2015b). To investigate the optical properties of the single-crystal samples, the steady-state photoluminescence (PL) has been measured in Figure 1E by using the 488-nm laser with an intensity of 10 μW . The strong PL peak locates at 545 nm, and the corresponding optical bandgap can be calculated as 2.2 eV, which matches well with the reported single-crystal MAPbBr₃ (Saidaminov et al., 2015b).

To investigate the position response of the device, we built a custom-designed optoelectronic test platform to provide a focused laser beam with intensity ranging from 0.13 to 22 μW (see Transparent Methods section for more details). The related instruments included the Raman spectrometer, portable probe station, and KEITHLEY 2614B SourceMeter. The photoresponse of the device was measured under the illumination of the focused laser with a wavelength of 553 nm (spot size \sim 5 μm) with the laser spot moving in a direction perpendicular to the perovskite channel.

When the photoelectric characteristics were measured, the laser was focusing on the channel boundary of the MAPbBr₃ device as the initial position ($X = 0 \mu\text{m}$, shown in Figure 1C, where X represents the photosensing distance and is defined as the distance between the center of the laser spot and the perovskite channel boundary and the yellow circles represent the positions of focused beam). Figure 2A exhibits the laser-intensity-dependent I - V curves of the perovskite photodetector ($X = 0 \mu\text{m}$; $\lambda = 553 \text{ nm}$), in which the light intensity is defined as the laser intensity on the surface of crystal. It shows that the photocurrent improves gradually on promoting the laser intensity from 0.13 to 22 μW , and a high photoexcited current

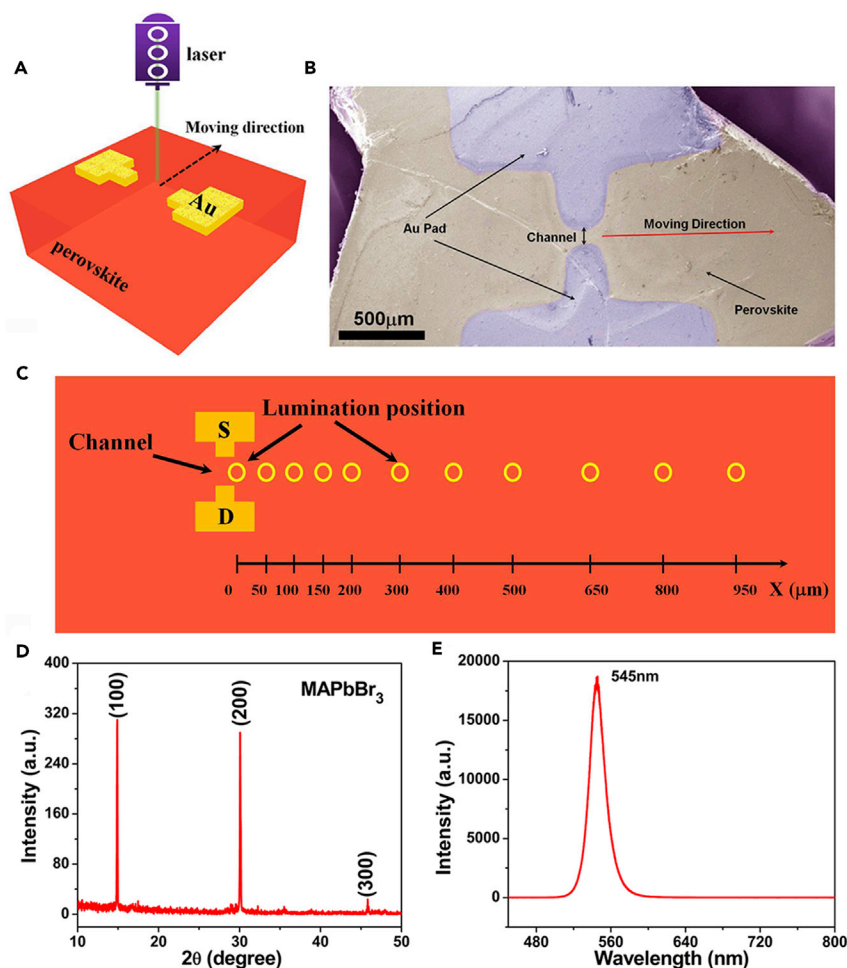


Figure 1. Single-Crystal Perovskite Photodetector with Long-Range Position Dependence

(A) Schematic of the device and the position-dependent photoresponse measurement setup (laser spot size: 5 μm).
 (B) Scanning electron micrograph of the MAPbBr₃-based photodetector.
 (C) The position of laser illumination (yellow circles) on the device, where X denotes the distance of the illumination position from the boundary of the perovskite channel.
 (D) X-ray diffraction of ground MAPbBr₃.
 (E) Photoluminescence spectrum of the MAPbBr₃ crystals.

can be obtained as 220 nA ($V_{\text{bias}} = -10$ V) when the laser power is 22 μW . Furthermore, all plots are approximately straight, indicating a good Ohmic contact between the Au electrode and perovskite. Figure 2B gives the corresponding relationship between the photocurrent and laser intensity at a bias voltage of 10 V, which indicates that the laser intensity and the photocurrent have a nonlinear relationship. The responsivity is an important parameter for photodetector, and it can be defined as $R = (I_{\text{ph}} - I_{\text{dark}}) / P_{\text{opt}}$, where I_{ph} is the photocurrent, I_{dark} is the dark current, and P_{opt} is the laser intensity. The optimal responsivity for the perovskite photodetector can be obtained as 51 mA/W. Figure 2C shows the time response of the perovskite photodetector, which is measured by periodically turning on and off a 535-nm laser at a bias voltage of 10 V ($X = 0$ μm ; $P = 22$ μW). The result indicates that the device exhibits good stability switching properties, and the photocurrent to dark current ratio can be calculated as 9 (see Figure S2 for more details of photoresponse under different wavelengths of light illumination). The detailed raise time and fall time can be observed in Figure 2D as 3.5 and 0.1 s, respectively. After the laser irradiation, the photocurrent increases very fast, and then gradually rises, which is attributed to the slow raise time. The main reason for this is that water gas and oxygen molecules are adsorbed on the MAPbBr₃ surface, creating a passivation layer with low conductivity. Upon illumination, the photogenerated holes (the main carrier in MAPbBr₃) (Dong et al., 2015a) are affected by the passivation layer produced by water gas and oxygen on the surface,

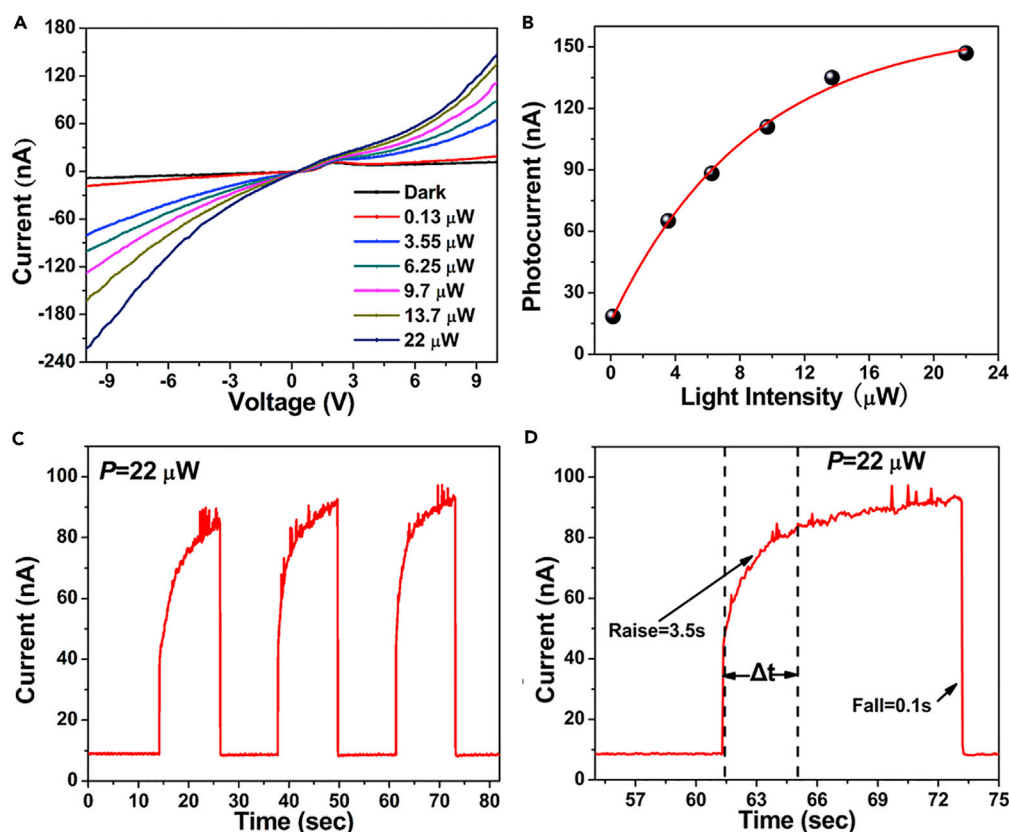


Figure 2. Basic Performance of Single-Crystal Perovskite Photodetector

- (A) I - V characteristics of the devices under 553 nm with different light intensities at $X = 0\ \mu\text{m}$.
 (B) The plot of photocurrent versus light intensity at $V = 10\text{ V}$ ($\lambda = 553\text{ nm}$; $X = 0\ \mu\text{m}$).
 (C) Time response of the device illuminated with and without a 553-nm laser (22 μW ; $X = 0\ \mu\text{m}$) at a voltage of 10 V.
 (D) The amplified sections of a 61–63.5 s range and 72–74 s range corresponding to light-off to light-on and light-on to light-off transitions from Figure 2C.

resulting in a decrease in the holes carrier concentration and gradual increase of photocurrent raise time (Hu et al., 2012). Hence, the time performance of the photodetector can be significantly improved by vacuum encapsulation.

To further investigate the position-dependent photoresponse of the device, we measured the I - V curves when focusing the laser spot at a different position X away from the channel boundary both in dark condition and under the 553-nm laser with a laser power of 22 μW , as shown in Figure 3A. It can be seen that the photocurrent decreases gradually with the laser spot away from the channel from 0 to 950 μm with an effective photo-sensing distance up to millimeter range, which is beyond the record of previous reports (shown in Table 1). Besides, the performances of two other samples are shown in Figure S1 to prove the repeatability of the experiment. It is obvious that all the three devices demonstrated position-dependent photo-detection performance up to millimeter range. The dependence of photocurrent and responsivity (R) on focused distance for devices is exhibited in Figure 3B ($P = 22\ \mu\text{W}$, $V = 10\text{ V}$). A high photocurrent and responsivity of 147 nA and 6.1 mA/W, respectively, can be obtained at the initial position ($X = 0$, $P = 22\ \mu\text{W}$) and then decreases with the increase of distance. This phenomenon is related to the carriers' diffusion in perovskite single crystals. Upon 532-nm laser illumination, plenty of carriers can be generated in the MAPbBr₃ device. When the illumination position (X) is far away from the initial position, a few photo-generated carriers can diffuse into the channel as the effect of recombination. Hence, the photocurrent gradually decreases with the increase of X . Besides, the change ratio in photocurrent and responsivity become smaller when the focused distance is larger than 200 μm . These phenomena are related to the initial diffusion distribution of the photo-generated carriers before applying the electric field. Some of the diffused carriers are closer to the edge of the electrode when the light spot is closer to the channel

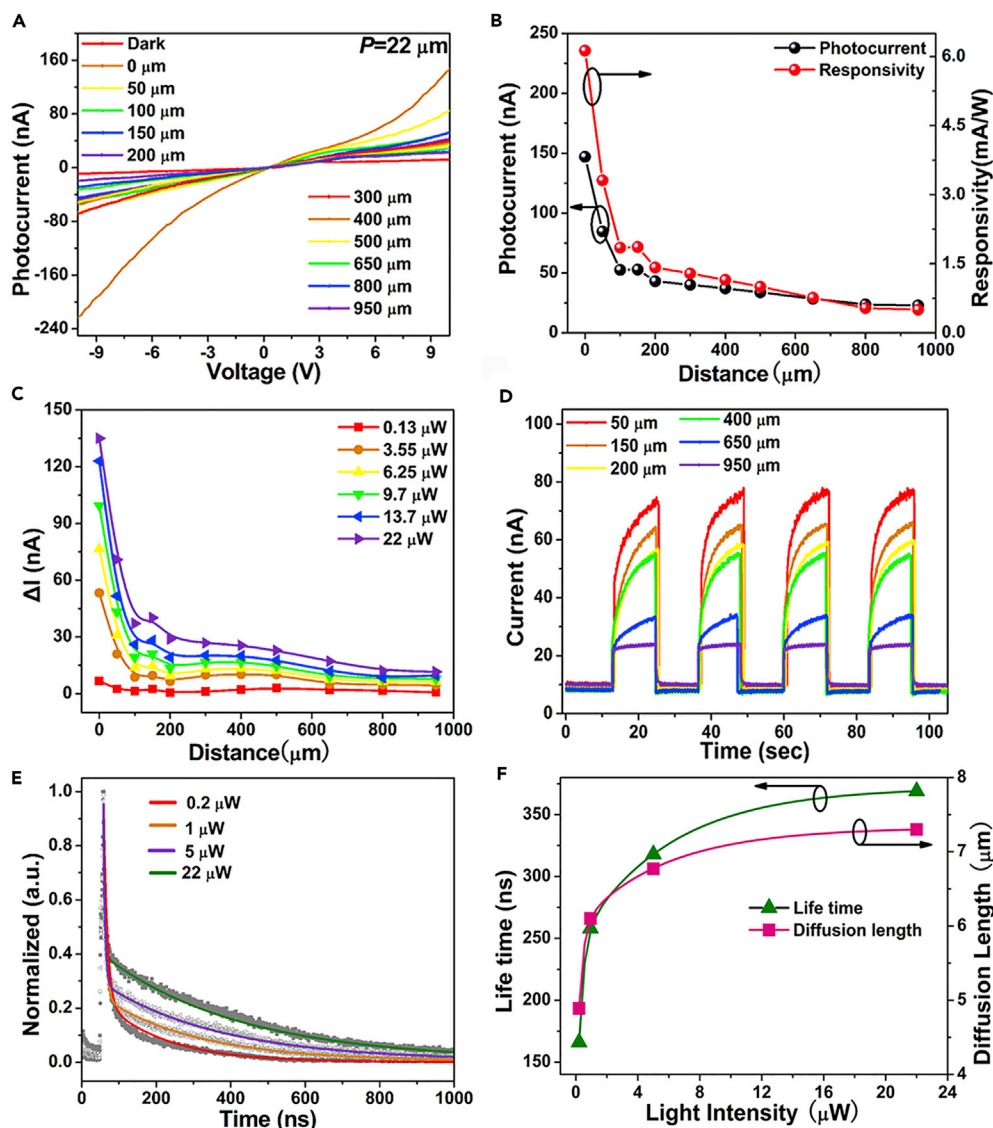


Figure 3. Position-Dependent Photodetection Properties

(A) *I*-*V* curves of the photodetector as a function of distance ranging from 0 to 950 μm under 553-nm laser with an intensity of 22 μW.

(B) Photocurrent and responsivity as a function of distance at voltage of 10 V ($P = 22 \mu\text{W}$).

(C) The plots of the dependence of ΔI ($\Delta I = I_{\text{Photocurrent}} - I_{\text{Darkcurrent}}$) on the illumination position, measured at different incident intensities ($V = 10 \text{ V}$).

(D) Time response of the device under different illumination positions ($\lambda = 553 \text{ nm}$; $P = 22 \mu\text{W}$; $V = 10 \text{ V}$).

(E) Time-resolved photoluminescence of MAPbBr₃ single crystal under different laser intensities.

(F) Fitting carrier lifetime and diffusion length under different laser intensities from Figure 3E.

region, which contributes more current by shorter travel path for degeneration. Such effect is discussed in detail in following Discussion section and Supplemental Information. To appraise the photodetection ability of the device for position and laser intensity, photocurrent response was characterized under the illumination of the 553-nm laser with intensity range from 0 to 22 μW at different positions. As Figure 3C depicts, all photocurrents of different laser powers gradually decrease with the illumination position increasing from 0 to 950 μm under a bias of 10 V. The ΔI ($I_{\text{Photocurrent}} - I_{\text{Darkcurrent}}$) of relatively weaker laser intensity declines faster than that of relatively stronger laser intensity due to the relatively smaller carrier lifetime under the weaker light, which matches the measurement of carrier lifetime and carrier diffusion length well (shown in Figures 3E and 3F). This indicates that the position dependence profile of the position-dependent

Materials	Carriers Diffusion Length	Coupling Efficiency	On-Off Ratio	Longest Photo-sensing Distance	Reference
Graphene/SiC	<3 μm	<100%	2.5	500 μm	Sarker et al. (2017)
Reduced graphene oxide	<100 nm	100%	2.93	Within the channel	Ghosh et al. (2010)
Perovskite single crystals	7.3 μm	100%	9	950 μm	This work

Table 1. Comparison between Previous Position-Dependent Photodetectors and This Work

photodetector can be tuned by laser intensity. More details about time-resolved PL fitting method are shown in Figure S4 in part 3 of the Supplemental Information. The time-dependent photocurrent exhibits a similar photoresponse as the previous single-crystal perovskite and good stability properties (~ 70 nA) when the illumination ($P = 22 \mu\text{W}$) is focused on the device ($X = 50 \mu\text{m}$), as shown in Figure 3D. As the distance increases to 950 μm , a much smaller photocurrent can be observed (~ 22 nA) and is slower compared with the initial position (~ 147 nA). Meanwhile, the repeatability for different positions is also very good. Interestingly, we found that the corresponding raise time of the perovskite device increased from 3.5 to 6.9 s as the focused distance gradually increased under illumination of 22 μW , which shows a tendency to that of photocurrent (shown in Figure S3). We found that it is mostly attributed to electrode structure, as shown in Figure 1B. In the region close to the channel, the total distance carriers traveled increases more rapidly as the light spot moves out far away from the region. Thus, the rapid decrease in the relatively smaller distance can account for our rapidly growing corresponding response time in the region near the channel.

DISCUSSION

A numerical model was developed to explain the position-dependent photoresponse. Figure 4A schematically shows the operation mechanism of the photodetector, in which the carriers drift along the direction of the electric field line. The model assumes that the OTP response is determined by the photo-generated charge carriers that transported under the electric field from the photoexcitation region to the edge of the electrode.

Thus, the density of the photo-generated holes p' (x , t) can be calculated via the following differential equation:

$$D_h \frac{\partial^2 p'}{\partial x^2} - \mu_h \varepsilon_0 \frac{\partial p'}{\partial x} - \frac{p'}{\tau} + G_{\text{ext}} = \frac{\partial p'}{\partial t} \quad (\text{Equation 1})$$

where p' is the density of the photo-generated holes, D_h is the diffusion coefficient of the holes, μ_h is the mobility of the holes, ε_0 is the mean electric field, τ is the lifetime of the carriers, and G_{ext} is the photo-generated rate of the carriers.

A rigorous view of the situation can be obtained by writing the homogeneous differential equation that controls steady-state minority carrier behavior in the following way:

$$\frac{d^2 p'}{dx^2} - \frac{1}{L_\varepsilon} \frac{dp'}{dx} - \frac{p'}{L_h^2} = 0 \quad (\text{Equation 2})$$

where $L_h = \sqrt{D_h \tau}$ is the mean diffusion length and $L_\varepsilon = \frac{kT}{q\varepsilon_0}$ is the mean length that a carrier diffuses into an electric field. Solutions to this equation are of the form: $p'(x) = K_1 e^{\frac{x}{L_1}} + K_2 e^{\frac{x}{L_2}}$, where L_1 and L_2 are the roots of the characteristic equation:

$$L_\varepsilon L^2 + L_h^2 L - L_\varepsilon L_h^2 = 0 \quad (\text{Equation 3})$$

According to the above equation, there are two characteristic scale lengths in a general problem (L_1 and L_2), which both exhibit a mixture of drift and diffusion. For high electric field values (similar to our experiments), L_1 is reduced as E^{-1} , whereas the absolute value of L_2 increases as E . L_1 can be considered as a generalized diffusion length, or the mean distance that carriers diffuse in the perovskite single crystal.

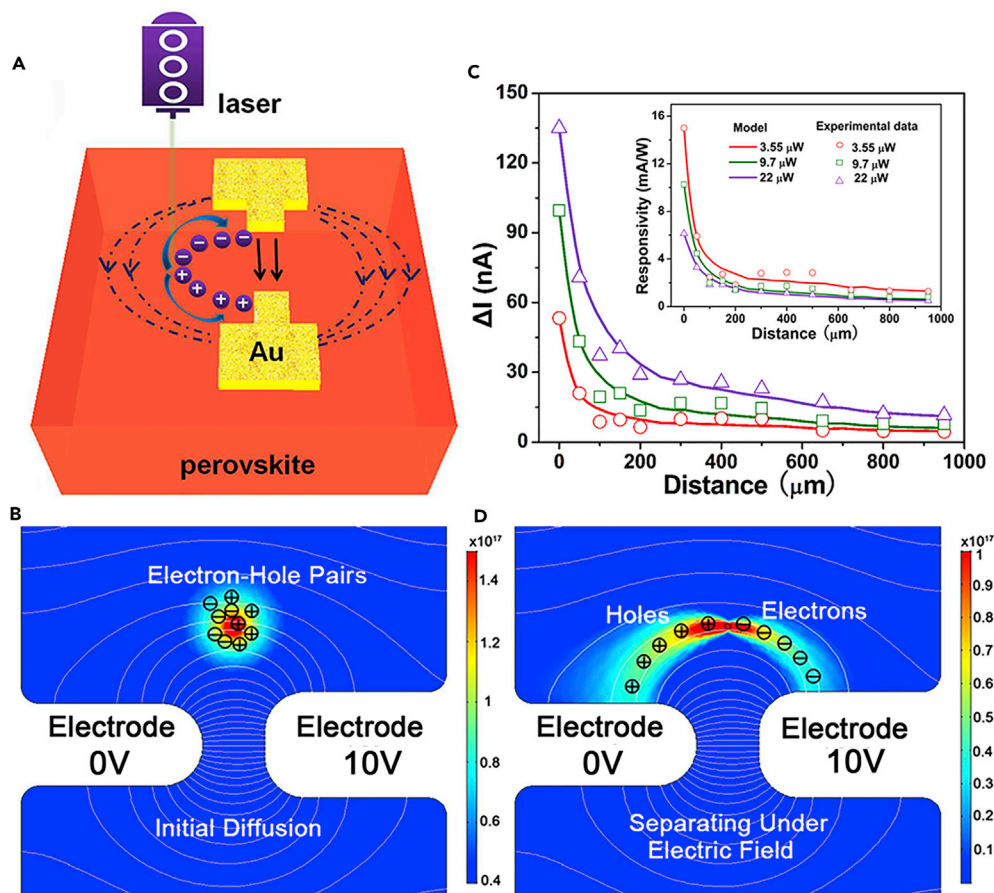


Figure 4. Operation Mechanism and Numerical Simulation of the Photodetector

(A) Schematic of the operation mechanism of the position-dependent photodetector.

(B and D) (B) The distribution of electric potential and electric field using finite-element analysis. (D) The white line in the figure is the electric field line, and the trajectory of the electron and hole is nearly the same as the electric field line.

(C) The simulation curve of the photoresponsivity. The dark simulation curve fits the nonlocal position-dependent photoresponsivity data well.

L_2 can be considered as a generalized recombination length, or mean distance that the carriers travel in the perovskite single crystal before recombination. Since the reciprocal sum of lifetimes implies that the smallest lifetime dominates the generation/recombination dynamics of semiconductors $\frac{1}{\tau_{\text{eff}}} = \frac{1}{\tau_1} + \frac{1}{\tau_2}$. The smallest characteristic scale length dominates the carriers' degeneration as well. Thus, the effective degeneration length L_{eff} , which combines the diffusion and the recombination effect in the single-crystal OTPs in our model, can be calculated through the reciprocal sum of the two characteristic lengths as $\frac{1}{L_{\text{eff}}} = \frac{1}{L_1} + \frac{1}{L_2}$.

Considering the total distance carriers traveled d_{total} , a fraction of charge carriers escape degeneration and reach the vicinity of the electrode from the illumination position with a transport factor given by $T = \exp\left(-\frac{d_{\text{total}}}{L_{\text{eff}}}\right)$ (Sarker et al., 2017). In our model, such transport factor can be estimated by the following formula (see the Supplemental Information for more details of the deformation for the formulas):

$$T(x, y) = \exp\left(-\frac{\varphi(x, y)}{K \times E(x, y)^\alpha}\right) \quad (\text{Equation 4})$$

where $\varphi(x, y)$ is the normalization electric potential value at the position that carriers generated, $E(x, y)$ is the normalization electric field value at the position the same as $\varphi(x, y)$, and K is a normalization parameter in this model. The parameter α ($0 < \alpha < 2$) is the experimental ideality factor to describe the combining effect of diffusion and recombination in our model, which is further discussed in the Supplemental

Information. The distribution of the electric potential and the electric field are both calculated using finite-element analysis. Figure 4B demonstrates the initial distribution of the carriers' diffusion after light excitation (Del Alamo, 2009). Figure 4D shows that electrons and holes move toward the electrode under the action of an electric field. The white line in the figure is the electric field line, and the trajectories of the electron and hole are both along the electric field line.

The number of charges transported to the vicinity of the electrode is the product of the normalization average transport factor $\overline{T(x)}$ and the number of the photo-generated charges in the OTPs, which is related to the incident light intensity. Thus, the photocurrent generated (induced change of current between source and drain) and the photoresponsivity can be described as the following formulas:

$$I_{\text{photo}}(x) = \beta(p) \overline{T(x)} \quad (\text{Equation 5})$$

$$R_{\text{mod}}(x) = \frac{I_{\text{photo}}(x)}{p} \quad (\text{Equation 6})$$

where $\beta(p)$ is the current generated factor related to the incident light intensity (p), which is discussed in the Supplemental Information. The normalization average transport $\overline{T(x)}$ is calculated by considering the initial diffusion of the photo-generated carriers before applying an electric field, which is relevant to the diffusion length (see Figure S5 in part 4 in the Supplemental Information for more details). The photoresponsivity predicted by the model demonstrates the photocurrent and responsivities under different laser intensities (Figure 4C), which explains the nonlocal position-dependent photoresponsivity data well (see Figure S6 in the Supplemental Information for more details discussion of parameter α). It can be noticed that after the distance increases to 200 μm , the degeneration of the photo-generated current becomes slower. It can be attributed to the decrease of the degeneration of the electric field when the distance increases over 200 μm due to the electrode shape. Such effect is considered in our model, and our fitting result comes out well. The simulated results for different α are also shown in the Supplemental Information. The diffusion effect dominates in the OTPs when the parameter α is close to zero, which indicates that OTPs are desirable for position-sensitive photodetection applications.

In summary, we proposed a position-dependent and millimeter-range photodetector based on perovskite single crystals. As a demonstration, the position-sensitive photoresponse characteristics of the photodetector was measured by scanning a focus laser beam over the device perpendicular to the perovskite channel. The photoresponsivity and photocurrent decreased from 6.1 to 0.5 and 147 to 22 nA, respectively, when the focused beam position varied from 0 to 950 μm . With the focus beam position varying from 0 to 950 μm , the photocurrent and response time changed from 147 to 20 nA and 3.5 to 6.9 s, respectively. When X is larger than 200 μm , the ratio of the decline of the photocurrent, responsivity, and response time become much gentle due to the change of carriers' travel paths at different positions. The attenuation of carrier diffusion length in MAPbBr_3 with the decrease of the exciting laser was demonstrated by positional photocurrent characterization. This phenomenon indicates the tunable position dependence profile of position-dependent photodetector. Due to the combined influence of carriers' drift and diffusion under an electric field, a numerical model was developed to explain the field effect photodetection mechanism and the experimental observation of position-dependent photocurrent characteristics for our devices. This position-dependent photodetector presents a prototype of single material system with large effective photo-sensing distance, opening up a new path for the design of novel light detection device for future intelligence optoelectronic system.

METHODS

All methods can be found in the accompanying Transparent Methods supplemental file.

SUPPLEMENTAL INFORMATION

Supplemental Information includes Transparent Methods and six figures and can be found with this article online at <https://doi.org/10.1016/j.isci.2018.08.021>.

ACKNOWLEDGMENTS

This work was supported by National Key R&D Program (2016YFA0200400), National Natural Science Foundation (61574083, 61434001, 61874065, 11474277, 11434010), National Basic Research Program (2015CB352101), Special Fund for Agro-Scientific Research in the Public Interest of China (201303107), Beijing Natural Science Foundation (4184091), and Research Fund from Beijing Innovation Center for Future

Chip. The authors are also thankful for the support of the Independent Research Program of Tsinghua University (2014Z01006) and Shenzhen Science and Technology Program (JCYJ20150831192224146).

AUTHOR CONTRIBUTIONS

Conceptualization, T.-L.R. and H.T.; Methodology, Y.-T.L., G.-Y.G., L.-S.L., and X.-S.G.; Investigation, Y.-T.L., G.-Y.G., L.-S.L., and Z.-Y.J.; Experiments, Y.-T.L., G.-Y.G., L.-S.L., and X.C.; Writing – Original Draft, Y.-T.L., G.-Y.G., L.-S.L., and Y.T.; Writing – Review & Editing, Y.-T.L. and H.T.; Funding Acquisition, T.-L.R., Y.Y., and P.-H.T.; Resources, T.-L.R., and P.-H.T.; Supervision, T.-L.R., and H.T.

DECLARATION OF INTERESTS

The authors declare no competing interests.

Received: June 2, 2018

Revised: August 4, 2018

Accepted: August 27, 2018

Published: September 28, 2018

REFERENCES

- Bi, Y., Hutter, E.M., Fang, Y., Dong, Q., Huang, J., and Savenije, T.J. (2016). Charge carrier lifetimes exceeding 15 μ s in methylammonium lead iodide single crystals. *J. Phys. Chem. Lett.* **7**, 923–928.
- Del Alamo, J.A. (2009). *Integrated Microelectronic Devices: Physics and Modeling* (Pearson Education).
- Dong, Q., Fang, Y., Shao, Y., Mulligan, P., Qiu, J., Cao, L., and Huang, J. (2015a). Electron-hole diffusion lengths > 175 μ m in solution-grown $\text{CH}_3\text{NH}_3\text{PbI}_3$ single crystals. *Science* **347**, 967–970.
- Dong, R., Fang, Y., Chae, J., Dai, J., Xiao, Z., Dong, Q., Yuan, Y., Centrone, A., Zeng, X.C., and Huang, J. (2015b). High-gain and low-driving-voltage photodetectors based on organolead triiodide perovskites. *Adv. Mater.* **27**, 1912–1918.
- Dou, L., Yang, Y.M., You, J., Hong, Z., Chang, W.-H., Li, G., and Yang, Y. (2014). Solution-processed hybrid perovskite photodetectors with high detectivity. *Nat. Commun.* **5**, 5404.
- Fang, Y., Dong, Q., Shao, Y., Yuan, Y., and Huang, J. (2015). Highly narrowband perovskite single-crystal photodetectors enabled by surface-charge recombination. *Nat. Photonics* **9**, 679–686.
- Fang, Y., and Huang, J. (2015). Resolving weak light of sub-picowatt per square centimeter by hybrid perovskite photodetectors enabled by noise reduction. *Adv. Mater.* **27**, 2804–2810.
- Ghosh, S., Sarker, B.K., Chunder, A., Zhai, L., and Khondaker, S.I. (2010). Position dependent photodetector from large area reduced graphene oxide thin films. *Appl. Phys. Lett.* **96**, 163109.
- Green, M.A., Ho-Baillie, A., and Snaith, H.J. (2014). The emergence of perovskite solar cells. *Nat. Photonics* **8**, 506–514.
- Hu, L., Yan, J., Liao, M., Xiang, H., Gong, X., Zhang, L., and Fang, X. (2012). An optimized ultraviolet-a light photodetector with wide-range photoresponse based on ZnS/ZnO biaxial nanobelt. *Adv. Mater.* **24**, 2305–2309.
- Hu, X., Zhang, X., Liang, L., Bao, J., Li, S., Yang, W., and Xie, Y. (2014). High-performance flexible broadband photodetector based on organolead halide perovskite. *Adv. Funct. Mater.* **24**, 7373–7380.
- Kang, D.H., Pae, S.R., Shim, J., Yoo, G., Jeon, J., Leem, J.W., Yu, J.S., Lee, S., Shin, B., and Park, J.H. (2016). An ultrahigh-performance photodetector based on a perovskite-transition-metal-dichalcogenide hybrid structure. *Adv. Mater.* **28**, 7799–7806.
- Lee, Y., Kwon, J., Hwang, E., Ra, C.H., Yoo, W.J., Ahn, J.H., Park, J.H., and Cho, J.H. (2015). High-performance perovskite-graphene hybrid photodetector. *Adv. Mater.* **27**, 41–46.
- Li, F., Ma, C., Wang, H., Hu, W., Yu, W., Sheikh, A.D., and Wu, T. (2015). Ambipolar solution-processed hybrid perovskite phototransistors. *Nat. Commun.* **6**, 8238.
- Liu, C., Wang, K., Du, P., Wang, E., Gong, X., and Heeger, A.J. (2015a). Ultrasensitive solution-processed broad-band photodetectors using $\text{CH}_3\text{NH}_3\text{PbI}_3$ perovskite hybrids and PbS quantum dots as light harvesters. *Nanoscale* **7**, 16460–16469.
- Liu, C., Wang, K., Yi, C., Shi, X., Du, P., Smith, A.W., Karim, A., and Gong, X. (2015b). Ultrasensitive solution-processed perovskite hybrid photodetectors. *J. Mater. Chem. C* **3**, 6600–6606.
- Ma, C., Shi, Y., Hu, W., Chiu, M.H., Liu, Z., Bera, A., Li, F., Wang, H., Li, L.J., and Wu, T. (2016). Heterostructured $\text{WS}_2/\text{CH}_3\text{NH}_3\text{PbI}_3$ photoconductors with suppressed dark current and enhanced photodetectivity. *Adv. Mater.* **28**, 3683–3689.
- Mao, Y., Banerjee, S., and Wong, S.S. (2003). Large-scale synthesis of single-crystalline perovskite nanostructures. *J. Am. Chem. Soc.* **125**, 15718–15719.
- Miyata, A., Mitioglu, A., Plochocka, P., Portugall, O., Wang, J.T.-W., Stranks, S.D., Snaith, H.J., and Nicholas, R.J. (2015). Direct measurement of the exciton binding energy and effective masses for charge carriers in organic-inorganic tri-halide perovskites. *Nat. Phys.* **11**, 582–587.
- Qian, L., Sun, Y., Wu, M., Xie, D., Ding, L., and Shi, G. (2017). A solution-processed high-performance phototransistor based on a perovskite composite with chemically modified graphenes. *Adv. Mater.* **29**, 1606175.
- Saidaminov, M.I., Abdelhady, A.L., Murali, B., Alarousu, E., Burlakov, V.M., Peng, W., Dursun, I., Wang, L., He, Y., and Maculan, G. (2015a). High-quality bulk hybrid perovskite single crystals within minutes by inverse temperature crystallization. *Nat. Commun.* **6**, 7586.
- Saidaminov, M.I., Adinolfi, V., Comin, R., Abdelhady, A.L., Peng, W., Dursun, I., Yuan, M., Hoogland, S., Sargent, E.H., and Bakr, O.M. (2015b). Planar-integrated single-crystalline perovskite photodetectors. *Nat. Commun.* **6**, 8724.
- Sarker, B.K., Cazalas, E., Chung, T.-F., Childres, I., Jovanovic, I., and Chen, Y.P. (2017). Position-dependent and millimetre-range photodetection in phototransistors with micrometre-scale graphene on SiC. *Nat. Nanotechnol.* **12**, 668.
- Shao, Y., Xiao, Z., Bi, C., Yuan, Y., and Huang, J. (2014). Origin and elimination of photocurrent hysteresis by fullerene passivation in $\text{CH}_3\text{NH}_3\text{PbI}_3$ planar heterojunction solar cells. *Nat. Commun.* **5**, 5784.
- Shi, D., Adinolfi, V., Comin, R., Yuan, M., Alarousu, E., Buin, A., Chen, Y., Hoogland, S., Rothenberger, A., and Katsiev, K. (2015). Low trap-state density and long carrier diffusion in organolead trihalide perovskite single crystals. *Science* **347**, 519–522.
- Stranks, S.D., Eperon, G.E., Grancini, G., Menelaou, C., Alcocer, M.J., Leijtens, T., Herz, L.M., Petrozza, A., and Snaith, H.J. (2013). Electron-hole diffusion lengths exceeding 1

micrometer in an organometal trihalide perovskite absorber. *Science* **342**, 341–344.

Wang, Y., Zhang, Y., Lu, Y., Xu, W., Mu, H., Chen, C., Qiao, H., Song, J., Li, S., and Sun, B. (2015). Hybrid graphene-perovskite phototransistors with ultrahigh responsivity and gain. *Adv. Opt. Mater.* **3**, 1389–1396.

Wei, H., Fang, Y., Mulligan, P., Chiriac, W., Fang, H.-H., Wang, C., Ecker, B.R., Gao, Y., Loi, M.A., and Cao, L. (2016). Sensitive X-ray detectors

made of methylammonium lead tribromide perovskite single crystals. *Nat. Photonics* **10**, 333.

Xia, H.-R., Li, J., Sun, W.-T., and Peng, L.-M. (2014). Organohalide lead perovskite based photodetectors with much enhanced performance. *Chem. Commun.* **50**, 13695–13697.

Xing, G., Mathews, N., Sun, S., Lim, S.S., Lam, Y.M., Grätzel, M., Mhaisalkar, S., and Sum, T.C. (2013). Long-range balanced electron-and hole-

transport lengths in organic-inorganic $\text{CH}_3\text{NH}_3\text{PbI}_3$. *Science* **342**, 344–347.

Yang, Y., Yan, Y., Yang, M., Choi, S., Zhu, K., Luther, J.M., and Beard, M.C. (2015). Low surface recombination velocity in solution-grown $\text{CH}_3\text{NH}_3\text{PbBr}_3$ perovskite single crystal. *Nat. Commun.* **6**, 7961.

Zhang, W., Eperon, G.E., and Snaith, H.J. (2016). Metal halide perovskites for energy applications. *Nat. Energy* **1**, 16048.

ISCI, Volume 7

Supplemental Information

Millimeter-Scale Nonlocal Photo-Sensing

Based on Single-Crystal

Perovskite Photodetector

Yu-Tao Li, Guang-Yang Gou, Lin-Sen Li, He Tian, Xin Cong, Zhen-Yi Ju, Ye Tian, Xiang-Shun Geng, Ping-Heng Tan, Yi Yang, and Tian-Ling Ren

1. Transparent Methods

Synthesis of Perovskite single crystals: The MAPbBr₃ single crystals were synthesized via an anti-solvent method with slight modification (Shi et al., 2015). In briefly, 0.734 g PbBr₂ and 0.269 g CH₃NH₃Br were dissolved in 2 mL N, N-dimethylformamide (DMF). Subsequently, 2 mL CH₂Cl₂ as anti-solvent was diffused into perovskite solution slowly, and then small single crystals (~1-2 mm in size) precipitate out. For large crystal growth, by placing the small crystal into fresh solution and repeating the above process, larger crystal (~ 4 mm) was formed.

Fabrication of position-dependent photodetector: Perovskite single crystals (MAPbBr₃) was synthesized through solution process. Then hard mask with defined patterning was covered on the surface of the MAPbBr₃ and fixed by the polyimide tape. Finally, 50 nm Au electrodes were made by conventional electron beam evaporation to define shaped source and drain with a channel of 150 μm width and 120 μm length.

Performance measurement of the position-dependent photodetector: A custom-designed photoelectric measuring system was built by assembling three instruments: the Raman spectrometer, portable probe station, and KEITHLEY 2614B SourceMeter. A focused laser beam with the wavelength of 553 nm (spot size~5 μm) was introduced as the excitation sources, which moved in a direction perpendicular to the perovskite channel. The laser intensity was adjusted by the optical attenuator in the Raman spectrometer and was tested at the objective of the microscope before photodetection properties characterization. Two probes were connected to the Au electrodes to detect the signal. The current signal was recorded using KEITHLEY 2614B SourceMeter.

2.

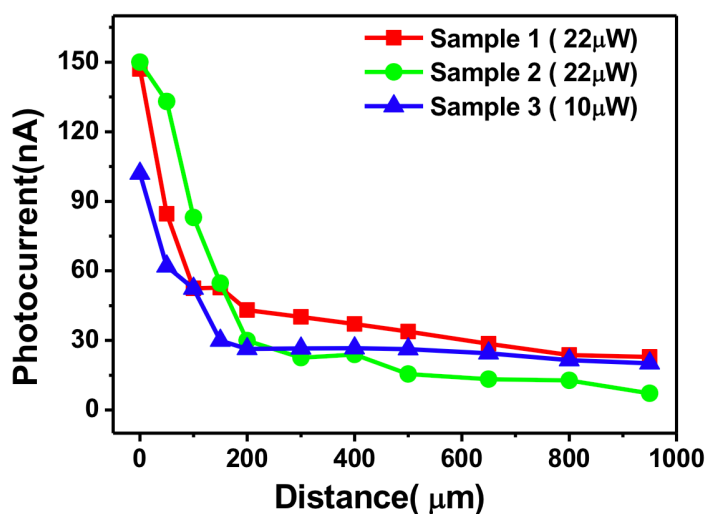


Figure S1. Photocurrents of the three samples as a function of distance at voltage bias of 10 V, related to Figure 3. The results proof the repeatability of the experiment is well. The devices were tested under the laser of 553 nm with laser power of 22 μW (Sample 1, 2) and 10 μW (Sample 3).

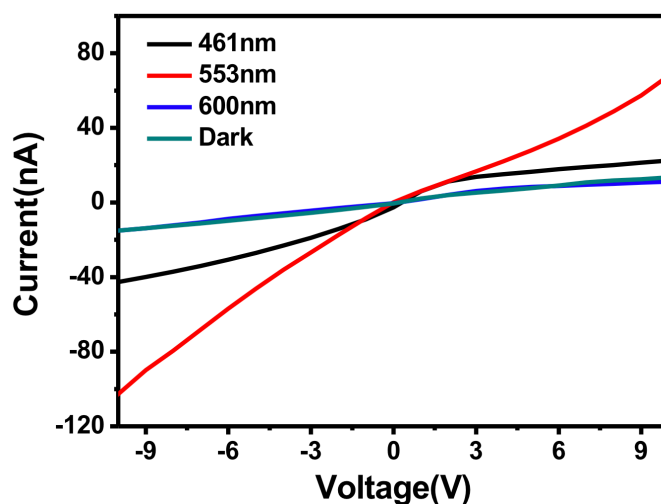


Figure S2. The photoresponse of sample 3 under different wavelengths of the light illumination (10 μW), related to Figure 2. The light current of the device increases with the wavelength approaching 553nm. When it reaches 600nm, the light current is almost the same as the dark current.

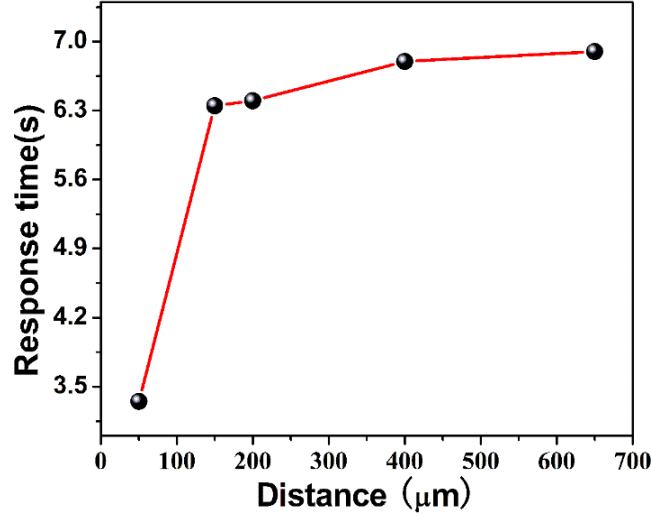


Figure S3. The corresponding raise time of the perovskite device (Sample 1), related to Figure 3. The raise time increases from 3.5 to 6.9 s as the focused distance gradually increased under illumination of 22 μW , which shows the opposite tendency compared to the photocurrent.

3. Calculation of carrier diffusion length

The diffusion length of the MAPbBr_3 single crystal can be determined by the following formula:

$$L_D = \left(\frac{k_B T \mu \tau_r}{e} \right)^{\frac{1}{2}} \quad (\text{S1})$$

where k_B , T , μ and e are the Boltzmann constant, absolute temperature, carrier mobilities, and elementary charge, respectively. τ_r is the carrier lifetime which can be acquired from time-resolved photoluminescence. (Shown in Figure 3e).

According to Mott-Gurney law, a trap-filling process is identified by the marked increase of the current injection at a bias range higher than 10 V in Figure S4, and the device dark current (J_D) is measured to derive carrier mobilities:

$$J_D = \frac{9 \epsilon \epsilon_0 \mu V_b^2}{8 L^3} \quad (\text{S2})$$

where L is the distance between the center of the two Au pads, ϵ ($= 32$) is the relative dielectric constant of MAPbBr₃, and ϵ_0 is the vacuum permittivity. V_b is the applied voltage. Large hole mobility of $51.3 \text{ cm}^2 \text{ S}^{-1} \text{ V}^{-1}$ is derived from the curve fitting. Hence, the diffusion length calculated from the two formulas is $7.3 \text{ }\mu\text{m}$, which matches the previous report well (Saidaminov et al., 2015). Besides, According to the operation instructions (version 3.4.0) of EDINBURGH PHOTONICS company, the fitting curve of time-resolved photoluminescence of MAPbBr₃ single crystal under different laser intensity was acquired, Thus, we can get the fitting carrier lifetimes and the diffusion lengths under different laser intensities in Figure 3f from above methods.

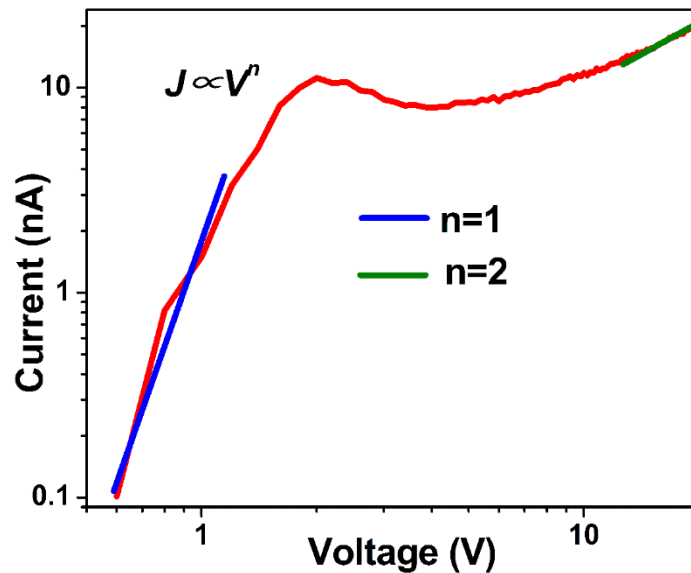


Figure S4. The dark current-voltage curve for a MAPbBr₃ device, related to **Figure 3**. The result is well fitted (green line) by the Mott-Gurney law (Dong et al., 2015).

4. Nonlocal photo-response measured and model simulation

The simulation suggests that our model can explain the observed position dependent photo-response experimental data quite well. Here we provide an in-depth discussion of our model organization. The flowchart of our model simulation is shown as followed:

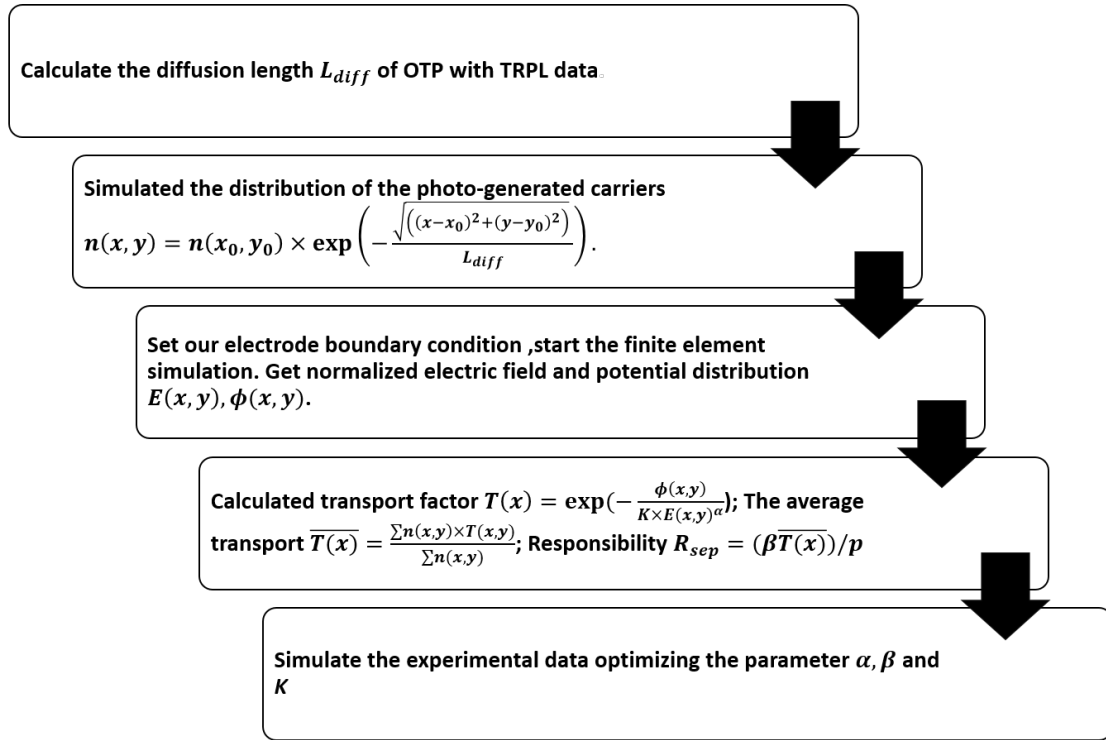


Figure S5. The flowchart of our model simulation, related to Figure 4. The flowchart describes the five steps of the device performance simulation.

The average transport factor is calculated considering the initial diffusion carriers before applying the electric field. Within the circle with radius of $r_{max} = 50 \mu\text{m}$, we consider the initial photo-generated distribution as an exponential damping $n(x, y) = n(x_0, y_0) \times \exp\left(-\frac{\sqrt{(x-x_0)^2 + (y-y_0)^2}}{L_{diff}}\right)$. Here, x_0 and y_0 are coordinate of the circle center where the laser spots on. L_{diff} is the diffusion length of the MAPbBr₃ single crystal, calculated in the main text. So, we can calculate the average transport factor $T(x)_{avg} = \frac{\sum_{r < r_{max}} n(x, y) \times T(x, y)}{\sum_{r < r_{max}} n(x, y)}$. To simplify our simulation, we can normalize the average transport factor $\overline{T(x)}_0$ with $\overline{T(0)}_0$ (the average transport factor at $x = 0 \mu\text{m}$), where the photo-generated current is the largest. Consequently, there is the normalization average transport factor $\overline{T(x)} = \frac{T(x)_{avg}}{T(0)_{avg}}$ in our model. But the distribution of $T(x, y)$ is still needed in our model for $T(x)_{avg}$ calculation (Sarker et al., 2017).

$$T(x, y) = \exp\left(-\frac{d_{total}}{L_{eff}}\right) = \exp\left(-\int_0^\varphi \frac{d\varphi}{EL_{eff}}\right) \quad (S3)$$

$$\frac{1}{L_{eff}} = \frac{1}{L_1} + \frac{1}{L_2} \quad (S4)$$

where E and φ are the electric field and electric potential along the direction of the electric field line. There are two characteristic scale lengths in a general problem, L_1 and L_2 . They both exhibit a mixture of drift and diffusion. For high electric field values, L_1 is reduced as E^{-1} , while the absolute value of L_2 increases as E , which both exhibit a mixture of drift and diffusion (Del Alamo, 2009). Hence, we can also introduce an experimental ideality factor $0 < \alpha < 2$ in our model combining the effect of diffusion and recombination. Such parameter α will also include the nonlinearity introduced by the non-uniform electrical field. Consequently, we can simplify the contribution of different carriers as shown in the main text by the following formulas:

$$\frac{1}{EL_{eff}} = C1 \times \left(\frac{E}{E_0}\right)^0 + C2 \times \left(\frac{E}{E_0}\right)^{-2} = C \times E(x, y)^{-\alpha} \quad (S5)$$

$$T(x, y) = \exp\left(-\frac{\varphi(x, y)}{K \times E(x, y)^\alpha}\right); \quad \varphi(x, y) = \frac{\varphi}{\varphi_0} \quad (S6)$$

where the normalization constants ($E_0 = 1 \text{ V/m}$, $\varphi_0 = 1 \text{ V}$) are used to simplify the calculation by changing the electric field to the absolute value. $\varphi(x, y)$ is the normalization electric potential value (the relative electric potential value compared to the potential of 1V) at the position that carriers generated; $E(x, y)$ is the normalization electric field value (the relative electric field value compared to the potential of 1V/m) at the position the same as $\varphi(x, y)$. K is a normalization parameter in this model.

As the α is close to 0, L_1 has more contribution on the L_{eff} . L_1 is considered as generalized diffusion length, the mean distance that the carrier diffuses in the bulk of a semiconductor. Consequently, if the α is close to 0 when fitting on the experimental data, the diffusion process will have much greater contribution than the recombination process during the carriers transport in such materials. The simulated results for different α are also shown as followed. As the distance increases, we can observe that the photocurrent generated will have a quicker drop when the α is closer

to 0. We can fit the experimental data to get such parameter α to determine the contribution of the diffusion and the recombination during the transport.

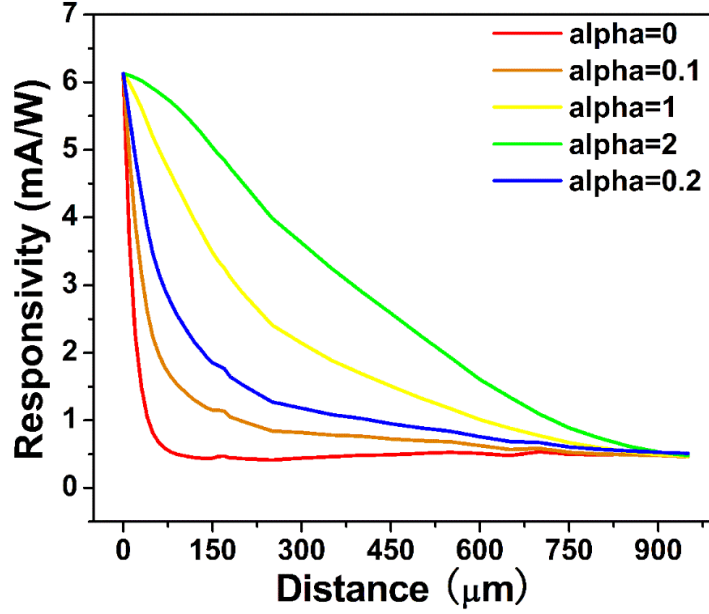


Figure S6. The simulated responsivities for different α parameters, related to **Figure 4**. The generated photocurrent will have a quicker drop when the α is closer to zero.

After fitting the experimental data with different incident laser intensities, it can be observed that the parameter α should become smaller to fit the curve with lower incident laser power, which means that the diffusion process has much more contribution than the recombination process when the incident power decreases. It can be attributed to the lower net recombination rate, which indicates that the recombination process has less contribution than the situation with high power incident laser. Since the net recombination rates are proportional to the excess np carriers product due to the band-to-band optical process, which is lower as the incident power decreased. As a result, we are expected to apply smaller α parameter to fit our experimental data well as the incident laser declined.

$$I_{\text{photo}}(x) = \beta(p)\overline{T(x)} \quad (S7)$$

For the photocurrent simulation formulas, the $\beta(p)$ is the current generated factor related to the incident laser power p . The nonlinearity photocurrents generation of the MAPbBr₃ at $x=0$ μm under different incident laser powers are shown in Figure 2(b) in the main text. In our calculation, we take the photocurrents generated at $x = 0$ μm as our current generated factor $\beta(p)$. $\overline{T(x)}$ is the normalization average transport factor which will be one at $x = 0$ μm . Consequently, our model can calculate the photocurrents in different locations and our results are good.

Thus the simulation parameters $\{\alpha, K, \beta(p)\}$ are $\{0.1, 0.23, 53.3 \text{ nA}\}$, $\{0.15, 0.165, 99.5 \text{ nA}\}$ and $\{0.2, 0.14, 135 \text{ nA}\}$ for different incident light intensities at 3.55, 9.7 and 22 μW , respectively. The simulation results are shown in the Figure 4c in the main text.

Supplemental References

Del Alamo, J.A. (2009) *Integrated Microelectronic Devices: Physics and Modeling*. (Pearson Education).

Dong, Q., Fang, Y., Shao, Y., Mulligan, P., Qiu, J., Cao, L., and Huang, J. (2015). Electron-hole diffusion lengths >175 μm in solution-grown CH₃NH₃PbI₃ single crystals. *Science* 347, 967–970.

Saidaminov, M.I., Adinolfi, V., Comin, R., Abdelhady, A.L., Peng, W., Dursun, I., Yuan, M., Hoogland, S., Sargent, E.H., and Bakr, O.M. (2015). Planar-integrated single-crystalline perovskite photodetectors. *Nat. Commun.* 6, 8724.

Sarker, B.K., Cazalas, E., Chung, T.-F., Childres, I., Jovanovic, I., and Chen, Y.P. (2017). Position-dependent and millimetre-range photodetection in phototransistors with micrometre-scale graphene on SiC. *Nature. Nanotech.* 12, 668.

Shi, D., Adinolfi, V., Comin, R., Yuan, M., Alarousu, E., Buin, A., Chen, Y., Hoogland, S., Rothenberger, A., and Katsiev, K. (2015). Low trap-state density and long carrier diffusion in organolead trihalide perovskite single crystals. *Science* 347, 519–522.